Zinc Selenide Nanoribbons and Nanowires

Yang Jiang,[‡] Xiang-Min Meng,[†] Wing-Ching Yiu, Ji Liu, Jun-Xian Ding, Chun-Sing Lee, and Shuit-Tong Lee*

Center of Super-Diamond and Advanced Films (COSDAF) and Department of Physics and Materials Science, City University of Hong Kong, Hong Kong SAR, China

Received: June 5, 2003; In Final Form: November 10, 2003

Zinc selenide nanoribbons and nanowires were obtained using laser ablation of ZnSe pressed powders. Their formation appeared to follow the vapor−solid and vapor−liquid−solid growth mechanisms, respectively. The product was characterized by means of scanning electron microscopy, transmission electron microscopy, micro-Raman scattering, and energy-dispersive X-ray spectroscopy. The ZnSe nanoribbons had a perfect wurtzite-2H single-crystal structure with a [120] growth direction and the {001} close-packed lattice planes of hexagonal ZnSe stacking along the nanoribbon width axis. The ZnSe nanowires grew with the {001} close-packed lattice planes of the wurtzite-2H structure stacking along the nanowire length axis. Both the longitudinal optic (LO) and transverse optic (TO) phonon peaks of the ZnSe nanowires and nanoribbons showed a clear shift toward low frequency relative to bulk values, probably because of small size and large surface effects. The ZnSe nanostructures exhibited strong self-activated luminescence centered at 596 nm.

Introduction

Wide-gap II−VI semiconductors are efficient emitters in the blue to ultraviolet spectral region, and excitons in these compounds are much more stable than those in the conventional III−V semiconductors that are widely used for optoelectronic applications.[1,2] Recent studies showed that the low-dimensional nanostructures of Zn-based II−VI wide-gap semiconductors exhibit exciton binding energies exceeding their optical phonon energies. As a consequence, the quantum yield of the II−VI-based devices is expected to be comparable to or greater than that of the common III−V devices. This advantage makes the nanoscale II−VI materials distinct from the III−V materials with respect to important applications for optoelectronics.[3,4] As a Zn-based II−VI compound, ZnSe is a direct band gap semiconductor, with a room-temperature band gap energy and an emission at 2.8 eV. This suggests that ZnSe is potentially a good material for short-wavelength lasers and other photoelectronic devices. Therefore, ZnSe is of great interest as a model material in such forms as thin films, quantum wells, and bulk crystals,[1,2,6−9] and ZnSe-based optoelectronic devices have been the subject of intensive research,[5]

In the pursuit of nanoelectronics, one-dimensional semiconductor nanostructures have attracted intense interest with regard to the fundamental issues concerning low dimensionality, space-confined transport, and device applications.[10] In recent years active research has focused on semiconductor wirelike nanostructures, including those of compound semiconductors (GaN,[11] GaAs,[12] InAs[13]), elemental semiconductors (Si,[14] Ge[15]), and oxide semiconductors (Ga_2O_3).[16] Compared to nanowires, nanoribbons,[17,18] which have a distinct rectangular cross section and a large width-to-thickness ratio, can offer exciting opportunities for both technological applications and fundamental research. Although a number of binary semiconductor oxide nanoribbons, such as ZnO, In_2O_3, Ga_2O_3, GdO,[18,19] and SnO_2,[20] have been synthesized, the only non-oxide nanoribbons reported are Si[17] and ZnS.[21] In this paper we report the synthesis of ZnSe nanoribbons and nanowires, as well as the microstructural characterization of these materials.

Experimental Section

The experiment setup consisted of a KrF pulsed excimer laser and a horizontal tube furnace with a quartz tube mounted inside. A target for laser ablation was made by pressing high-purity ZnSe powder (>99.9 wt %) at room temperature. The target was placed at one end of the quartz tube, and the silicon substrate coated with about 30 Å of gold film was put at the other end about 30 cm from the target. After the tube had been evacuated by a mechanical rotary pump to a pressure of 6×10^{-2} Torr, a carrier gas flow of argon premixed with 5% hydrogen was maintained at a rate of 50 sccm from the target end to the substrate end. The pressure inside the tube was maintained at 200 Torr by continuous pumping during the experiment. The temperature of the furnace at the central region was increased at a rate of 40 °C/min to 950 °C and held at this temperature. Before the experiment, a movable thermocouple was inserted in the tube to measure the temperature along the quartz tube. The temperatures at the location of the ablation target and silicon substrate were 700 and 800 °C, respectively. The KrF laser (wavelength of 248 nm, pulse width of 34ns, and energy of 450 mJ per pulse at 5 pulses per second) was then started and focused on the target. The laser ablation process lasted for 1 h.

Samples collected from the silicon substrates were characterized by scanning electron microscopy (SEM; Philips XL 30 FEG), transmission electron microscopy (TEM; Philips, CM20 operated at 200 kV), and high-resolution transmission electron microscopy (HRTEM; CM200 FEG, operated at 200 kV). Room-temperature photoluminescence (PL) spectra and Raman

* Author to whom correspondence and requests for materials should be addressed. E-mail: apannale@cityu.edu.hk.

[‡] Also affiliated with the Department of Materials Science and Engineering, Hefei University of Technology, Hefei, Anhui, China.

[†] Also affiliated with the Technical Institute of Physics and Chemistry, Chinese Academy of Sciences CAS, P. R. China.

10.1021/jp035595+ CCC: $27.50
Published on Web 02/06/2004

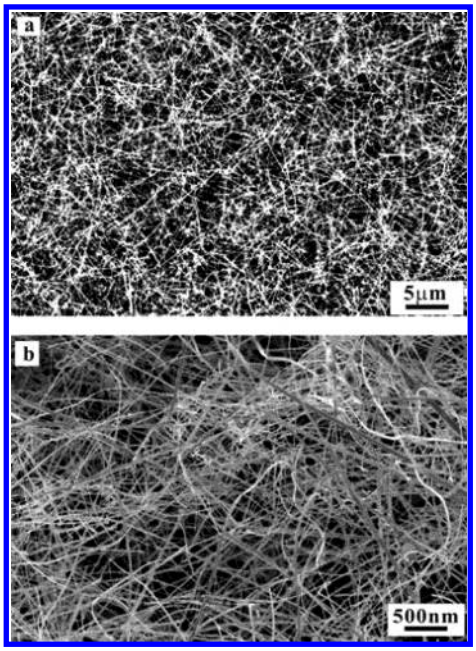

Figure 1. SEM images of the as-synthesized one-dimensional nanostructures at (a) low magnification and (b) high magnification.

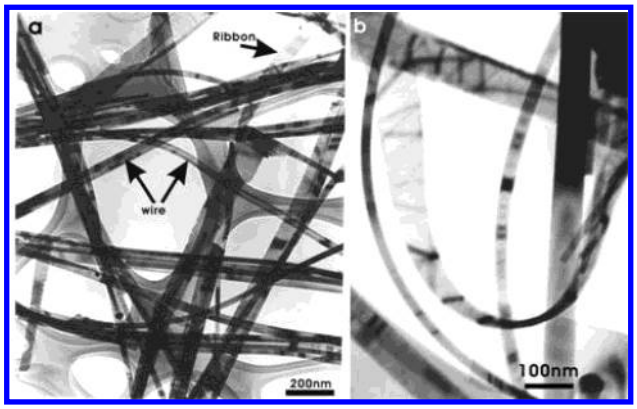

Figure 2. (a) Bright-field TEM image of ZnSe nanowires and nanoribbons and (b) bright-field TEM image of ZnSe nanoribbons at higher magnification.

scattering spectra were recorded with a Renishaw System 2000 spectrometer using the 514 nm line of Ar^+ for excitation.

Results and Discussion

The laser ablation resulted in the formation of a yellow wool-like product on the silicon substrate. Figure 1a shows that the product consists of a large quantity of wirelike structures with typical lengths in the range of 10−20 μm. A high-magnification SEM image (Figure 1b) reveals that the deposition product consists of both nanoribbons and nanowires in the ratio of about 40% to 60%, respectively. The typical width of the nanoribbons ranges from 50 to 80 nm. The formation of the yellow wool-like product, though not sensitive to the furnace temperature, always occurred at a location where the substrate temperature was about 800 °C. Although the length of the nanostructures was sensitive to the ablation time, the nanowire diameter and the nanoribbon width changed little when the ablation time was increased to 2 h or when the furnace center temperature was raised to 1050 °C.

The structure and morphology of the product were further characterized by TEM. Figure 2a shows a bright-field TEM image of the nanostructures, which confirms that the nanostructures consist of both nanowires and nanoribbons. The diameters of nanowires are in the range 20−30 nm. Each nanowire has a uniform diameter along the entire length. At higher magnification the TEM image of the nanoribbons (Figure 2b) shows that the curved nanoribbons have many dark streak (or striation) contrasts, which are bending contours due to lattice bending in thin crystals in the TEM sample. Their identity can be easily ascertained by tilting the TEM sample. The typical width and thickness of the nanoribbon is about 50 nm and less than 5 nm, respectively. Most nanoribbons have a uniform width along their entire length. The TEM observation also reveals that a spherical particle is present at one end of almost all of the nanowires but not in any of the nanoribbons. This suggests that the nanowires and nanoribbons likely form from different mechanisms. Energy-dispersive X-ray spectra (EDXS) showed that both the nanoribbons and the nanowires have the same composition. Other than the carbon and copper signals from the sample grid, Zn and Se are the only elements detected, and they are present in an atomic ratio close to 1:1.

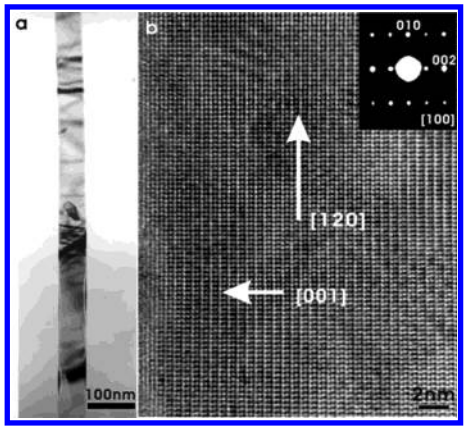

Figure 3. (a) Bright-field TEM image of a single ZnSe nanoribbon and (b) the corresponding high-resolution TEM image with the inset showing the [100] zone axis SAD pattern.

HRTEM images of an individual ZnSe nanoribbon and nanowire are shown in Figure 3 and Figure 4, respectively. Figure 3a is a typical bright-field TEM image of a nanoribbon; the corresponding HRTEM image and selected area diffraction (SAD) pattern are shown in Figure 3b and in the inset of Figure 3b, respectively. The SAD pattern and the lattice spacing (3.27 Å in the [002] direction) confirm that the nanoribbon is a 2H ZnSe single crystal with a growth direction along [120]. The flat surface of the nanoribbon is parallel to the (100) plane, whereas its width is in the [002] direction.

Figure 4a shows a typical bright-field TEM image of a ZnSe nanowire with a gold spherical particle at one end. The inset is the corresponding SAD pattern of the wire body. Figure 4b and Figure 4c show the HRTEM images of a region near the gold particle and in the wire body, respectively. The white arrows in Figure 4b and Figure 4c indicate the long direction of the wire. The SAD pattern and the HRTEM images confirm that the nanowire has a single-crystal structure matching that of the wurtzite-2H phase of ZnSe. The growth direction of the wire is along the [001] direction. Figure 4b also shows that the boundary between ZnSe and Au is very sharp. There are some stacking faults near the gold tip, which are rarely found in the ZnSe nanowire body.

The two different morphologies of ZnSe nanostructures suggest the existence of more than one growth mechanism. The metal sphere at the nanowire tip implies that the ZnSe nanowire growth is based on the well-known metal-catalytic vapor−liquid−solid (VLS) mechanism with gold as the catalyst and

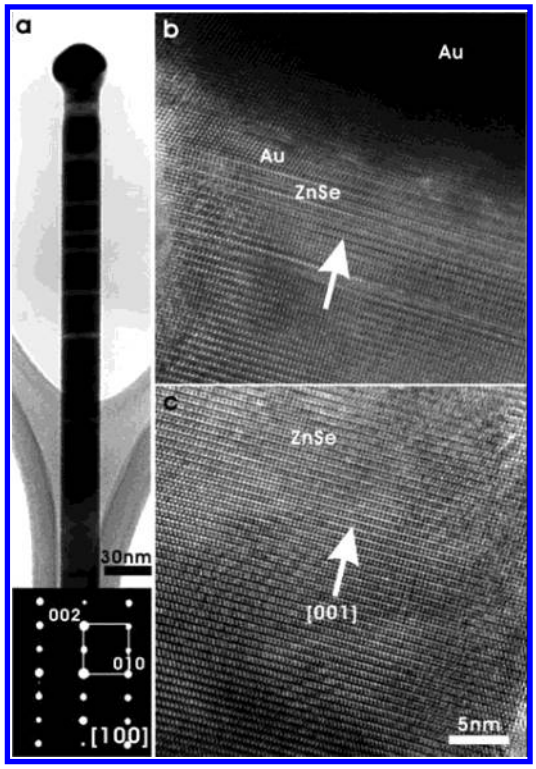

Figure 4. (a) Bright-field TEM image of single ZnSe nanowire with a gold tip, with the inset showing the [100] zone axis SAD pattern, (b) the corresponding HRTEM image of the region of the ZnSe nanowire near the tip, and (c) the corresponding HRTEM image of the ZnSe nanowire body.

the solvent at high temperature. The process starts with the dissolution of gaseous sources into nanometer-sized liquid gold droplets followed by nucleation and growth of the crystalline wires.[22] In our experiment, the ZnSe nanowire grew on Au-coated silicon substrate at about 800 °C. Zinc selenide vapor generated by laser ablation was transported by the carrier gas and then dissolved in the Au film to form a low-melting-point alloy. When the Zn atomic ratio in the solid solution exceeded 15%, the Au−Zn alloy's melting point would be less than 800 °C.[23] The Au alloy film would break into nanometer-sized liquid droplets, into which ZnSe vapor would continuously dissolve. When the concentration of ZnSe in the alloy solution became supersaturated at the substrate temperature, ZnSe crystal would precipitate. To minimize the interface energy, ZnSe would crystallize with its {001} close-packed planes aligned with the solid−liquid interface, leading to growth along the ⟨001⟩ direction.

On the other hand, similar to the oxide[18,20] and ZnS[21] nanoribbons, the nucleation and growth of ZnSe nanoribbons could be understood in terms of the vapor−solid mechanism. After the Au alloy film on the Si substrate broke into nanometer-sized liquid droplets, some bare Si regions would be exposed. In the present work, the ZnSe nanoribbons tended to nucleate and grow on the bare Si surface. Once nucleation started, the crystal ribbon will continue to grow epitaxially with ZnSe clusters being continuously supplied by the laser ablation process. This results in the preferential orientation of the ZnSe lattice planes as shown in Figure 3b. The phenomenon most likely originates from the anisotropic growth kinetics of the ZnSe crystal along different crystallographic directions as a result of the particular growth conditions that are responsible for the peculiar growth reported here.

To obtain Raman data for the different ZnSe nanostructures, the excitation laser was focused on different locations to select

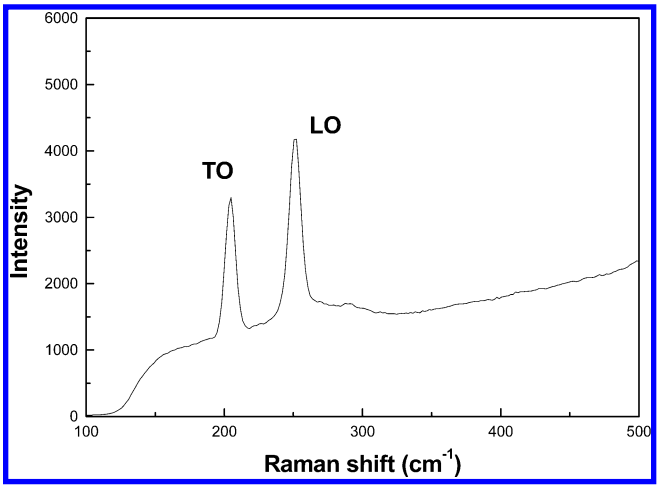

Figure 5. Room-temperature Raman spectrum of ZnSe nanostructures.

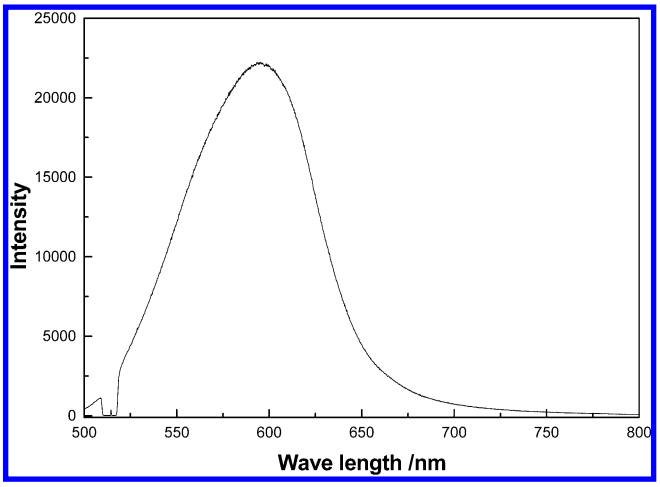

Figure 6. Room-temperature photoluminescence spectrum of ZnSe nanostructures.

either the nanowires or nanoribbons on the silicon substrate via an optical microscope. It is found that different regions containing primarily nanoribbons or nanowires had the same Raman spectrum. Figure 5 shows a typical room-temperature Raman spectrum of the ZnSe nanostructures. The Raman peaks at 203 and 250 cm^{-1} are attributed to the transverse optic (TO) and longitudinal optic (LO) phonon modes of ZnSe, respectively. No vibration modes due to impurities are observed. From previous reports,[24] the LO phonon frequency of single-crystalline ZnSe film is 254 cm^{-1} and that of single-crystal ZnSe is 255 cm^{-1} at room temperature. For ZnSe polycrystalline nanoparticles, the TO and LO phonon frequencies are 210 and 255 cm^{-1}, respectively, and both give a broad Raman peak due to the high surface-to-volume ratio of small particles. Compared to these results, the LO and TO phonon peaks of the ZnSe nanostructures are both shifted toward lower frequency, which is probably due to the effects of small size and high surface area. The relatively sharp and symmetric Raman peaks of the ZnSe nanostructures suggest that the ZnSe nanowires and nanoribbons are highly crystalline and single phase, which is in accord with the TEM observations shown above.

The same micro-Raman system was used to measure the PL spectra of the ZnSe nanostructures. Figure 6 shows a typical room-temperature PL spectrum of the ZnSe nanowires and nanoribbons, which exhibits a very strong and stable emission peak centered at 596 nm. In fact, the PL of ZnSe crystals or thin films is usually reported to occur at 442 nm for band gap emission or 500−560 nm for doped ion emission.[25] On the other

hand, the lower energy emission of about 2.08 eV from ZnSe microcrystals was assigned to self-activated luminescence, probably as a result of some donor−acceptor pairs related to Zn-vacancy and interstitial states.[26] Similarly, the strong emission from the present ZnSe nanostructures indicates the influence of Zn-vacancy and interstitial states, the nature of which is not clear or worthy of further study.

Conclusions

Zinc selenide nanoribbons and nanowires have been obtained using laser ablation of ZnSe powders. The growth of the nanoribbons and nanowires follows the vapor−solid and vapor−liquid−solid mechanism, respectively. The ZnSe nanoribbons have a perfect wurtzite-2H single-crystal structure with a [120] growth direction and the {001} close-packed lattice planes of hexagonal ZnSe stacking along the nanoribbon width axis. The ZnSe nanowires grow with the {001} close-packed lattice planes of the wurtzite-2H structure stacking along the nanowire length axis. Relative to the bulk crystals and polycrystalline nanoparticles of ZnSe, the LO and TO phonon peaks of the ZnSe nanowires and nanoribbons both shift toward lower frequencies, probably because of the effects of small size and high surface area. The strong self-activated luminescence centered at 596 nm has been observed in the ZnSe nanostructures. The successful synthesis of ZnSe and ZnS[21] nanostructures via laser ablation suggests that other II−VI non-oxide semiconductor nanostructures can be synthesized in a similar fashion as well.

Acknowledgment. This work is supported by the Research Grants Council of Hong Kong (CityU 3/01C, CityU 1294/03E), Hong Kong SAR, and the Chinese Academy of Sciences, China. Dr. Y. Jiang is also grateful for support from the Natural Science Foundation of Anhui Province, China (Grant No. 01044902).

References and Notes

(1) Gutowski, J.; Michler, P.; Ruckmann, H. I.; Breunig, H. G.; Rowe, M.; Sebald, K.; Voss, T. *Phys. Status Solidi B* **2002**, *234* (1), 70.

(2) Garcia, J. A.; Remon, A.; Zubiaga, A.; Munoz-Sanjose, V.; Martinez-Tomas, C. *Phys. Status Solidi A* **2002**, *194* (1), 338.

(3) Michler, P.; Vehse, M.; Gutowski, J.; Behringer, M.; Hommel, D.; Pereira, M. F.; Henneberger, K. *Phys. Rev. B* **1998**, *58*, 2055.

(4) Pereira, M. F.; Henneberger, K. *Phys. Rev. B* **1998**, *58*, 2064.

(5) Lischka, K. *Phys. Status Solidi B* **1997**, *202*, 673.

(6) Burov, L. I.; Ryabtsev, G. I.; Smal, A. S.; Waraxe, I. N. *Appl. Phys. B* **2002**, *75*, 63.

(7) Su, C.-H.; George, M. A.; Palosz, W.; Feth, S.; Lehoczky, S. L. *J. Cryst. Growth* **2000**, *213*, 267.

(8) Kato, H.; Udono, H.; Kikuma, I. *J. Cryst. Growth* **2001**, *229*, 79.

(9) Tournie, E.; Morhain, C.; Neu, G.; Faurie, J. P.; Triboulet, R.; Ndap, J. O. *Appl. Phys. Lett.* **1996**, *68*, 1356.

(10) Dekker, C. *Phys. Today* **1999**, *52*, 22.

(11) (a) Han, W. Q.; Fan, S. S.; Li, Q. Q.; Hu, Y. D. *Science* **1997**, *277*, 1287. (b) Duan, X. F.; Lieber, C. M. *J. Am. Chem. Soc.* **2000**, *122*, 188. (c) Chen, C. C.; Yeh, C. C. *Adv. Mater.* **2000**, *12*, 738. (d) Chen, C. C.; Yeh, C. C.; Chen, C. H.; Yu, M. Y.; Liu, H. L.; Wu, J. J.; Chen, K. H.; Chen, L. C.; Peng, J. Y.; Chen, Y. F. *J. Am. Chem. Soc.* **2001**, *123*, 2791.

(12) Duan, X. F.; Wang, J. F.; Lieber, C. M. *Appl. Phys. Lett.* **2000**, *76*, 1116.

(13) Li, H. X.; Wu, J.; Wang, Z. G.; Daniels-Race, T. *Appl. Phys. Lett.* **1999**, *75*, 1173.

(14) (a) Morales, A. M.; Lieber, C. M. *Science* **1998**, *279*, 208. (b) Yu, D. P.; Bai, Z. G.; Feng, S. Q.; Lee, C. S.; Bello, I.; Sun, X. S.; Tang, Y. H.; Zhou, G. W.; Zhang, Z. *Solid State Commun.* **1998**, *105*, 403. (c) Lee, S. T.; Wang, N.; Zhang, Y. F.; Tang, Y. H. *MRS Bull.* **1999**, *24*, 36. (d) Pan, Z. W.; Dai, Z. R.; Xu, L.; Lee, S. T.; Wang, Z. L. *J. Phys. Chem. B* **2001**, *105*, 2507.

(15) (a) Wu, Y.; Yang, P. *Chem. Mater.* **2000**, *12*, 605. (b) Zhang, Y. F.; Tang, Y. H.; Wang, N.; Lee, C. S.; Bello, I.; Lee, S. T. *Phys. Rev. B* **2000**, *61*, 4518.

(16) Choi, Y. C.; Kim, W. S.; Park, Y. S.; Lee, S. M.; Bae, D. J.; Lee, Y. H.; Park, G. S.; Choi, W. B.; Lee, N. S.; Kim, J. M. *Adv. Mater.* **2000**, *12*, 746.

(17) Shi, W. S.; Peng, H. Y.; Wang, N.; Li, C. P.; Xu, L.; Lee, C. S.; Lee, S. T.; *J. Am. Chem. Soc.* **2001**, 123, 11095.

(18) Pan, Z. W.; Dai, Z. R.; Wang, Z. L. *Science* **2001**, *291*, 1947.

(19) Dai, Z. R.; Gole, J. L.; Stout, J. D.; Wang, Z. L. *J. Phys. Chem. B* **2002**, *106*, 1274.

(20) Hu, J. Q.; Ma, X. L.; Shang, N. G.; Xie, Z. Y.; Wong, N. B.; Lee, C. S.; Lee, S. T. *J. Phys. Chem. B* **2002**, *106*, 3823.

(21) (a) Ma, C.; Moore, D.; Li, J.; Wang, Z. L. *Adv. Mater.* **2003**, *15* (3), 228. (b) Jiang, Y.; Meng, X. M.; Liu, J.; Xie, Z. Y.; Lee, C. S.; Lee, S. T. *Adv. Mater.* **2003**, *15* (3), 323.

(22) (a) Trentle, T. J.; Hickman, K. M.; Goel, S. C.; Viano, A. M.; Gibbons, P. C.; Buhro, W. E. *Science* **1995**, *270*, 1791. (b) Chen, C. C.; Yeh, C. C. *Adv. Mater.* **2000**, *12*, 738. (c) Shimada, T.; Hiruma, K.; Shirai, M.; Yazawa, M.; Haraguchi, K.; Sato, T.; Matsui, M.; Katsuyama, T. *Superlattices Microstruct.* **1998**, *24*, 435. (d) Wu, Y.; Yang, P. *Chem. Mater.* **2000**, *12*, 605.

(23) *Binary Alloy Phase Diagrams*, 2nd ed.; Massalski, T. B., Ed.; ASM International: Materials Park, OH, 1990; p 456.

(24) (a) Sarigiannis, D.; Peck, J. D.; Kioseoglou, G.; Petrou, A.; Mountziaris, T. J. *Appl. Phys. Lett.* **2002**, *80* (21), 4024. (b) Sarigiannis, D.; Peck, J. D.; Mountziaris, T. J.; Kioseoglou, G.; Petrou, A. *MRS Proc.* **2000**, *616*, 41. (c) Schreder, B.; Materny, A.; Kiefer, W.; Bacher, G.; Forchel, A.; Landwehr, G. *J. Raman Spectrosc.* **2000**, *31*, 959. (d) Lermann, G.; Bischof, T.; Materny, A.; Kiefer, W.; Kummell, T.; Bacher, G.; Forchel, A.; Landwehr, G. *J. Appl. Phys.* **1997**, *81* (3), 1446. (f) Mountaiaris, T. J.; Peck, J. D.; Stoltz, S.; Yu, W. Y.; Petrou, A.; Mattocks, P. G. *Appl. Phys. Lett.* **1996**, *68*, 2270.

(25) (a) Klude, M.; Hommel, D. *Appl. Phys. Lett.* **2001**, *79*, 2523. (b) Mazher, J.; Badwe, S.; Sengar, R.; Gupta, D.; Pandey, R. K. *Physica E* **2003**, *16*, 209.

(26) (a) Garcia, J. A.; Remon, A.; Zubiaga, A.; Sanjose, V. M.; Tomas, C. M. *Phys. Status Solidi A* **2002**, *194* (1), 338. (b) Suyver, J. F.; Wuister, S. F.; Kelly, J. J.; Meijerink, A. *Phys. Chem. Chem. Phys.* **2002**, *2*, 5445. (c) *Phosphor Handbook*; Shionoya, S., Yen, W. M., Eds.; CRC Press: Washington, DC, 1998; Chapter 3, pp 238−248.